ADVANCED FUNCTIONAL MATERIALS
www.afm-journal.de

Nanoarchitectured Graphene/CNT@Porous Carbon with Extraordinary Electrical Conductivity and Interconnected Micro/Mesopores for Lithium-Sulfur Batteries

Hong-Jie Peng, Jia-Qi Huang, Meng-Qiang Zhao, Qiang Zhang, Xin-Bing Cheng, Xin-Yan Liu, Wei-Zhong Qian, and Fei Wei**

The sp^2-hybridized nanocarbon (e.g., carbon nanotubes (CNTs) and graphene) exhibits extraordinary mechanical strength and electrical conductivity but limited external accessible surface area and a small amount of pores, while nanostructured porous carbon affords a huge surface area and abundant pore structures but very poor electrical conductance. Herein the rational hybridization of the sp^2 nanocarbon and nanostructured porous carbon into hierarchical all-carbon nanoarchitectures is demonstrated, with full inherited advantages of the component materials. The sp^2 graphene/CNT interlinked networks give the composites good electrical conductivity and a robust framework, while the meso-/microporous carbon and the interlamellar compartment between the opposite graphene accommodate sulfur and polysulfides. The strong confinement induced by micro-/mesopores of all-carbon nanoarchitectures renders the transformation of S_8 crystal into amorphous cyclo-S_8 molecular clusters, restraining the shuttle phenomenon for high capacity retention of a lithium-sulfur cell. Therefore, the composite cathode with an ultrahigh specific capacity of 1121 mAh g^{-1} at 0.5 C, a favorable high-rate capability of 809 mAh g^{-1} at 10 C, a very low capacity decay of 0.12% per cycle, and an impressive cycling stability of 877 mAh g^{-1} after 150 cycles at 1 C. As sulfur loading increases from 50 wt% to 77 wt%, high capacities of 970, 914, and 613 mAh g^{-1} are still available at current densities of 0.5, 1, and 5 C, respectively. Based on the total mass of packaged devices, gravimetric energy density of GSH@APC-S//Li cell is expected to be 400 Wh kg^{-1} at a power density of 10 000 W kg^{-1}, matching the level of engine driven systems.

1. Introduction

Motivated by the diverse nanostructures and high chemical stability of C–C covalent bonding, carbon materials have been widely utilized in various electrochemical energy storage systems.[1] On one aspect, the sp^2-hybridized carbon nanomaterials (e.g. one-dimensional (1D) carbon nanotubes (CNTs) and two-dimensional (2D) graphene) exhibit extraordinary mechanical strength, electrical conductivity, and enormous adaptability to different interfacial processes.[2] However, both the graphene sheets and CNTs prefer to pack together, leading to their limited external accessible surface area for ions and a small amount of micropores and mesopores as nanoreactors for ion/active electrode material reservoir. On the other aspect, the activated carbon and mesoporous carbon afford huge surface area (>1000 m^2 g^{-1} in most cases) and abundant pore structures, which give rise to their excellent capacitive performance.[3] However, the amorphous and sp^3-hybridized C–C bondings in these nanostructured carbon cause very poor electrical conductance, and the predominant endohedral surface results in the transfer limitation of electrolyte ions during rapid charge and discharge process. The full demonstration of the potential of nanocarbon materials for advanced energy storage, especially for their board applications in rechargeable batteries, is still a great challenge.

When carbon materials are employed as electrode materials for electrochemical energy storage, the following intrinsic characters are commonly required: (1) outstanding electrical conductivity for efficient conductive networks; (2) hierarchical interconnected micro-/mesopores as ion channels for supercapacitors and active phase reservoirs for ion storage; (3) robust mechanical properties to overcome the volume changes of electrodes; (4) remarkable thermal conductivity that promotes effective heat dissipation within a composite electrode, potentially enhancing the safety.[4] Neither sp^2 nanocarbon nor porous carbon can solely meet all the above mentioned requirements. A rational combination of the sp^2 nanocarbon (e.g. CNT, graphene) and nanostructured porous carbon (e.g., micro-/mesoporous carbon) with two or more levels from nanometer to macroscopic scale is highly desired to obtain hierarchical all-carbon nanoarchitectures with full inherited advantages of the

H.-J. Peng, Dr. J.-Q. Huang, Dr. M.-Q. Zhao, Prof. Q. Zhang, X.-B. Cheng, X.-Y. Liu, Prof. W.-Z. Qian, Prof. F. Wei
Beijing Key Laboratory of Green Chemical Reaction Engineering and Technology
Department of Chemical Engineering
Tsinghua University
Beijing 100084, China
E-mail: zhang-qiang@mails.tsinghua.edu.cn; wf-dce@tsinghua.edu.cn

DOI: 10.1002/adfm.201303296

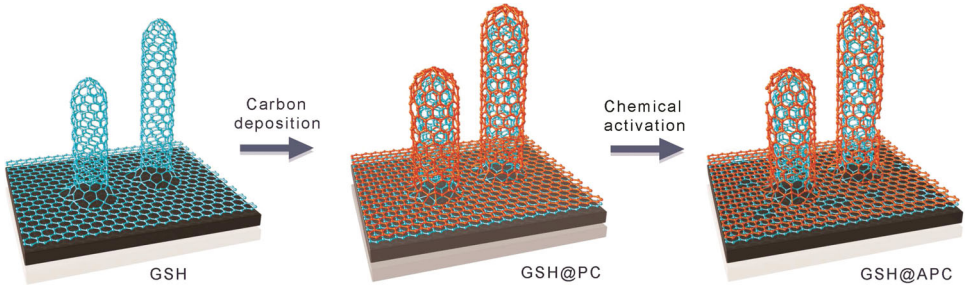

Scheme 1. Schematic illustration showing the nanoarchitectured graphene/CNT@porous carbon hybrid formation: The CVD grown GSHs were deposited with pyrolytic carbon into GSH@PC by CVI, then the KOH chemical activation of pyrolytic carbon into porous carbon for GSH@APC. The as-obtained hierarchical GSH@APC were of conductive network as well as large surface area and pore volume as cathode scaffold for Li–S batteries.

component materials or even with unexpected properties. For instance, hydrothermal CNT-containing carbon,[5] porous three-dimensional (3D) graphene-based nanocarbon,[6] the composite of CNTs as backbones in activated carbon matrix,[7] and mesoporous carbon walls within 3D interconnected macroporous graphene based frameworks[8] afford enhanced supercapacitive performance, such as high specific capacitance, good rate capability, and excellent cycling stability. Sulfur-doped porous carbons hybridized with graphene, in which the sulfur-doped porous carbons are uniformly distributed on both sides of the graphene sheets, offer high reversible capacity, a long cycle life, and excellent rate performances as electrode materials for supercapacitors[9] and lithium ion batteries.[10] Very recently, a composite carbon matrix with CNT-core/microporous-carbon-sheath structure is designed for metastable small sulfur accommodation, and the lithium-sulfur (Li-S) batteries based on such CNT@porous carbon composite exhibit high specific capacity, good cycling stability, and superior rate capability;[11] Another graphene–sulfur–carbon nanofibers coaxial nanocomposite was assembled as cathode for Li–S batteries with significantly improved cycle stability and capacity.[12] However, the CNTs/graphene might be flocculated into bundles or agglomerates because of strong van der Waals interactions during further mixing and casting procedures in the previously mentioned reports. The rational distribution of CNTs and/or graphene into carbon matrices with a well-designed structure and extraordinary energy storage performance is still a great challenge.

Recently, it has been shown that CNTs/graphene can be directly synthesized on various kinds of matrices to controllably fabricate nanocomposites.[13] If CNT/graphene can be controllably and uniformly hybridized by porous carbon, novel hierarchical carbon/carbon nanocomposites with well dispersed CNT/graphene could be available with anticipated performances for advanced energy storage. Generally, the formation of such hierarchical carbon/carbon nanocomposites requires self-organization of one carbon phase onto/into the other. If a 3D interconnected sp^2 carbon network is served as the scaffold, then the hybridization of porous carbon on such framework will lead to the fabrication of hierarchical all-carbon nanoarchitectures without degrading the electron pathway but rendering abundant interconnected meso-/micropores. Note that the graphene/single-walled CNT (SWCNT) hybrid has demonstrated to be a promising candidate as conductive scaffold due to its much more superior performance for Li–S batteries than other sp^2 nanocarbon such as multi-walled CNTs (MWCNTs), SWCNTs[14] and graphene[15] in our previous reports. Actually, SWCNTs in such architecture show much better performance in forming conducting network due to the lower defect density and higher conductivity. Based on this consideration, we explored the idea of in situ fabrication of porous carbon on an electrical conductive graphene/SWCNT framework. The as-obtained graphene/CNT hybrids encapsulated by porous carbon were employed as scaffolds to accommodate the sulfur, which afforded much improved Li-storage performance in discharge capacity and stability for Li–S battery applications.

Our concept involved the facile chemical vapor deposition (CVD) growth of graphene/SWCNT hybrids (GSHs), chemical vapor infiltration (CVI) of pyrolytic carbon (PC) for the fabrication of GSH@pyrolytic carbon (GSH@PC), and chemical activation by KOH for the fabrication of GSH@activated pyrolytic carbon (GSH@APC) hybrids, as illustrated in **Scheme 1**. Typically, 2D layered double oxide (LDO) catalyst was employed for catalytic CVD growth of GSHs. In the as-obtained hybrid, the SWCNTs interconnected with graphene planes through covalent C-C bonding and the interlinked SWCNTs with each other served as electrical conductive networks. Then, PC was in situ penetrated into the GSH framework by CVI of ethylene. Using KOH as the activating agent, the as-fabricated GSH@PC were chemically tailored into the GSH@APC, in which the GSHs served as the electron pathways, while the APCs afforded abundant micro-/mesopores as electrochemical reservoirs.

2. Results and Discussion

As shown in **Figure 1**a and S1, the GSH/LDOs that SWCNTs interlinked quasi-hexagonal graphene were synthesized on the surface of LDO flakes with catalytic CVD, in which process the LDO flakes served as 2D lamellar substrates for the formation of graphene while Fe nanoparticles generated on the hydrogen-reduced LDOs catalyzed the growth of SWCNTs synchronously. The graphene uniformly distributed on both sides of the flakes (Figure 1b), while the SWCNTs were interconnected with the graphene and extended on both sides of LDO flakes.[16] A d-spacing of 0.472 nm that corresponds to the (111) plane of $MgAl_2O_4$ spinel phase can be observed (Figure 1b), which was attributed to the topotactic transformation of layered double hydroxide (LDH) catalysts during

Adv. Funct. Mater. **2014**,
DOI: 10.1002/adfm.201303296

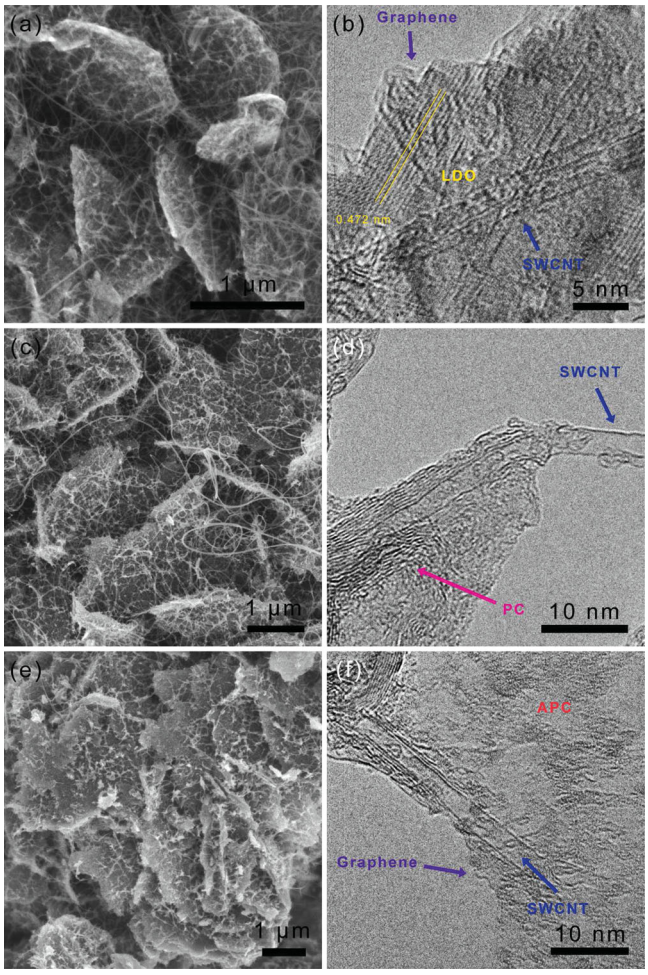

Figure 1. Morphologies of all-carbon hybrids: (a,b) GSH/LDO, (c,d) GSH@PC/LDO, and (e,f) GSH@APC.

calcination. Generally, the TEM images revealed that the GSHs were mainly composed of single-/few-layer (<4) graphene with a lateral size of 1–2 μm and SWCNTs with the length of several micrometers (Figure 1, S1 and S4). After the moderate ethylene pyrolysis, the as-obtained GSH@PC/LDO nanocomposites still remained the similar interlinked morphology (Figure 1c), while the surfaces of graphene and SWCNTs were surrounded by a turbostratic layer (Figure S2). Both the SWCNTs and graphene in the hybrids were coated with a disordered PC layer while the unique 1D cylindrical structure of nanotubes was preserved (Figure 1d). The GSHs have a very high sp^2-hybridized degree. In contrast, the PC has very small sp^2 domain and is full of edges and defects. Therefore, the PC prefers to react with KOH at a high temperature of 750 °C with the following reactions:[17]

$$2KOH \rightarrow K_2O + H_2O \quad (1)$$

$$C + H_2O \rightarrow CO + H_2 \quad (2)$$

$$CO + H_2O \rightarrow CO_2 + H_2 \quad (3)$$

$$CO_2 + K_2O \rightarrow K_2CO_3 \quad (4)$$

$$K_2O + H_2 \rightarrow 2K + H_2O \quad (5)$$

$$K_2O + C \rightarrow 2K + CO \quad (6)$$

Reaction of carbon with H_2O (formed along with K_2O by dehydration of KOH at deposited temperature) and the as-generated CO_2 were supposed to create large mesopores on PC; while at evaluated temperature above 700 °C, potassium metal formed by reaction of hydrogen gas or carbon with K_2O intercalated into the carbon lattice, expanded it, and was then quickly removed. This led to the generation of small mesopores (3.8–5.8 nm) and sub-nanometer micropores (0.6–1.1 nm), which is depended on the activating condition and the initial organization of carbon materials. Though various chemical activation method such as catalytic steam etching[18] and alkali activation[19] showed high efficiency in etching CNTs and graphene, the GSH scaffolds were well maintained during the KOH activation due to the higher graphitization degree, fewer edges, and lower defect density of GSH. The PC layers were much more active than the GSH frameworks under chemical activation. Therefore, the intact graphene flakes and tubular SWCNTs can be well preserved for GSH@APCs (Figure 1e, S3), while the PC layers on the surface of graphene and SWCNTs were chemically tailored by KOH (Figure 1f). Such selective reaction of GSH and PC with KOH endowed the GSH@APCs with electron pathways and porous nanostructures. An all-carbon GSH@APC nanocomposite was available after catalyst removal. As comparison, the GSH and GSH@PC without LDO substrates exhibited similar morphology of SWCNT interlinked graphene sheets but possessed less defects and small pores (Figure S4,5).

The textures and structural evolution of GSH to GSH@PC, and to GSH@APC were detailed characterized by thermogravimetry (TG), Raman spectroscopy, and N_2 sorption. It was shown that 1.21 g GSH was deposited on 1.0 g LDO catalyst. The content of PC in the as-obtained GSH@PC nanocomposites after the ethylene CVI was about 32.2 wt% (**Figure 2**a). After the removal of the catalyst flakes, the as-obtained GSH@APC nanocomposite exhibited a purity of over 97.0 wt%. From the differential TG (DTG) curve, the weight loss peaks of sequential GSH/LDO, GSH@PC/LDO, GSH@APC were shifted from 590 to 560, and to 407 °C, respectively, indicating the formation of turbostratic carbon by CVI and activated porous carbon in the nanocomposites that notably improved the reactivity with oxygen and reduced the thermal stability. A family of strong radial breathing mode peaks was detected in the Raman spectra for the original GSH, which became weak after the uniform deposition of turbostratic porous carbon (Figure 2b). This was ascribed to APC layers with abundant surface defects resulted by the ethylene CVI and the KOH activation covered the initial GSHs especially the neat SWCNTs, as indicated by the TEM characterization. Meanwhile, the mean I_D/I_G ratios (the intensity ratio of D peak around 1323 cm^{-1} and G peak around 1584 cm^{-1}, which correspond to disordered carbon and graphitic carbon bondings, respectively) of GSH@PC (0.88) and GSH@APC (0.90) were larger than that of GSH (0.68) as indicated in Figure S6.

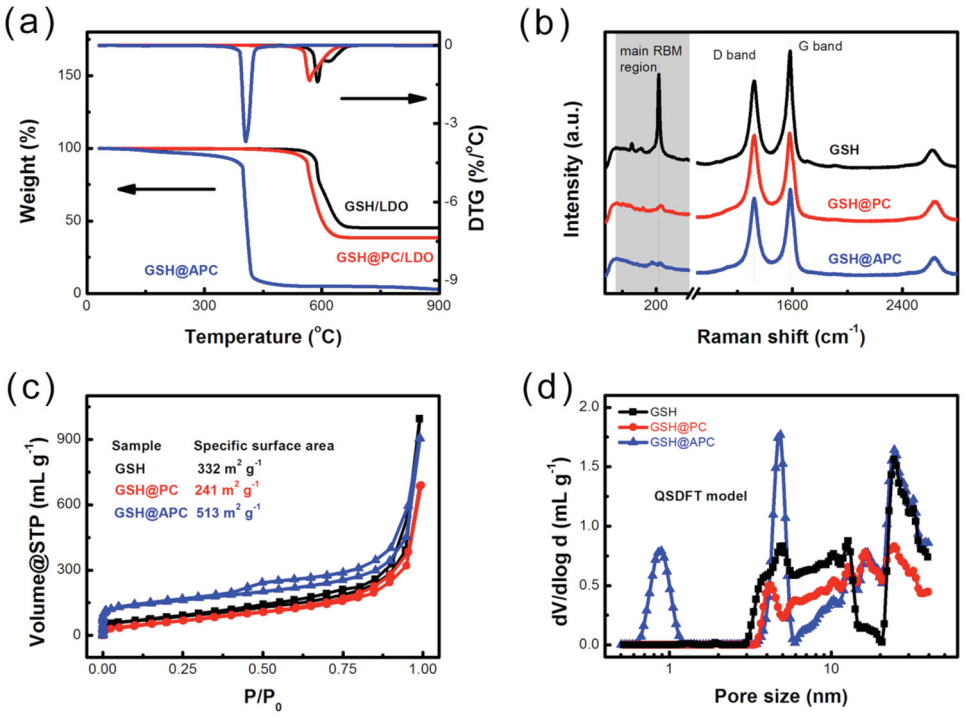

Figure 2. The characterization of all-carbon hybrids: (a) TG/DTG profiles of GSH/LDO, GSH@PC/LDO, and GSH@APC under O_2 atmosphere; (b) Raman spectra, (c) N_2 sorption isotherm and (d) pore size distribution based on QSDFT model of GSH, GSH@PC, and GSH@APC.

The N_2 sorptions of GSH and GSH@PC (Figure 2c) exhibited a type III adsorption isotherm with H3 hysteresis loop in IUPAC classification, indicating the unique adsorption behavior in the slit-shaped mesopores raised from the packing of graphene sheets. The N_2 sorption of GSH@APC illustrated an obvious increase at a very low P/P_0, which can be attributed to the introduction of micropores by KOH activation. The BET specified surface areas of GSH, GSH@PC, and GSH@APC were 332, 241, and 513 $m^2\ g^{-1}$, respectively. The pore size distributions of these samples calculated by quenched-solid density functional theory (QSDFT) were shown in Figure 2d and **Table 1**. The PC preferred to deposit in the pores with a size of 15–20 nm, leading to the decrease of the pore volume from 0.756 to 0.551 mL g^{-1}. After KOH activation, there was a large quantity of micropores with an average diameter of 0.89 nm, and the volume of which was sharply increased from 0 to 0.114 mL g^{-1}. A dual distribution of micropore at 0.6–1.1 nm and mesopore at 3.8–5.8 nm were observed on the GSH@APC. The electronic conductivities of the GSH, GSH@PC, GSH@APC were 4.34×10^3, 3.62×10^3, and 5.46×10^3 S m^{-1}, respectively (Figure S7 and Table 1). The as-fabricated GSH@APC nanocomposites remained the intact GSH structures that exhibited inherently high conductivity due to the fact that the mutually-assisted good dispersion of graphene and SWCNTs effectively avoided their stacking or agglomerating.

Among various energy storage devices, Li-S batteries are considered as one of the most promising candidates due to their very high theoretical energy density of 2600 Wh kg^{-1} (based on Li-S redox couple), high natural abundance, and environment friendly nature.[20] However, several intrinsic obstacles have to be well addressed before their realistic applications, including the ultra-low conductivity of element sulfur and lithium sulfide and the shuttling behavior of lithium polysulfides.[20,21] The use of sp^2 nanocarbon (CNTs,[14,22,23] graphene,[24–26] sp^2-carbon hybrid)[16], nanostructured carbon (mesoporous carbon,[27–29] porous hollow spheres,[30] hierarchical porous carbon)[31] as well as conductive polymer (polypyrrole,[32] polyacrylonitrile,[33] poly(3,4-ethylenedioxythiophene)-poly(styrene sulfonate))[34] to

Table 1. A summary of physical properties of hierarchical all-carbon nanoarchitectures.

Sample	Pore volume [mL g^{-1}]			Mean pore size [nm]		Conductance [S cm^{-1}]
	Micropore	Mesopore	Total	Micropore	Mesopore	
GSH	0.001	0.755	0.756	1.36	12.3	43.4
GSH@PC	0.000	0.551	0.551	–	15.0	36.2
GSH@APC	0.114	0.739	0.853	0.89	19.2	54.6
GSH@APC-S-50	0.000	0.250	0.250	–	20.5	29.3

DOI: 10.1002/adfm.201303296

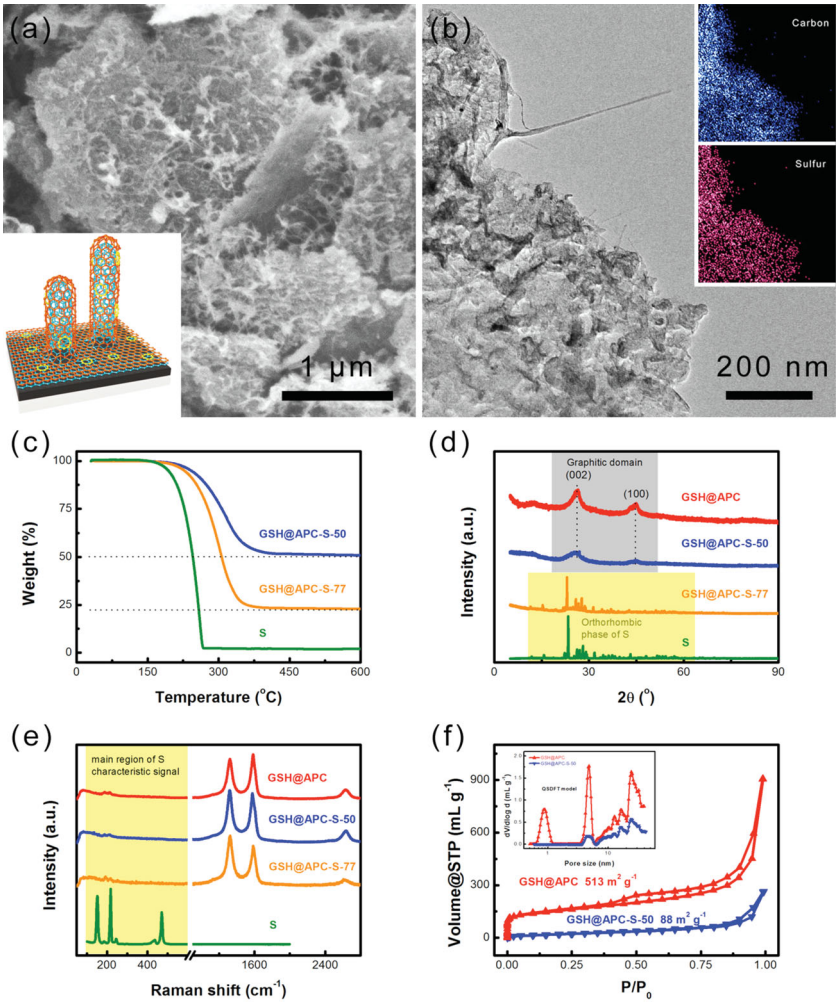

Figure 3. Structure of GSH@APC-S nanocomposites: (a) The SEM image, schematic illustration (inset figure) and (b) the TEM image, EDS mapping showing the distribution of element C and S (inset figure) of GSH@APC-S-50 nanocomposites; (c) TG profiles under N_2 atmosphere, (d) XRD patterns, (e) Raman spectra, (f) N_2 sorption isotherm, and pore size distribution (inset figure) of GSH@APC and GSH@APC-S-50 nanocomposites.

accommodate sulfur as sulfur composite cathodes have demonstrated enhanced capacity and stability of Li-S batteries. Herein, the all-carbon nanoarchitecture of GSH@APC was believed as excellent cathode materials for advanced Li-S batteries with abundant S-storage units composed of both porous APC-layers and the compartments between the two opposite graphene flakes. In detail, the GSH@APC-S nanocomposites were prepared through a facile melt-diffusion method at 155 °C, in which temperature liquefied S_8 with lowest viscosity was impregnated into the S-storage units as nanofillers through the strong capillary interaction. The as-obtained cathode still possessed the 3D-hybrid morphology with no obvious structural change after the sulfur impregnation and no bulk sulfur particles can be detected (**Figure 3**a). A desirable distributing status of S on the well-preserved carbon nanosheet was investigated by TEM and homologous EDS mapping of element C/S (Figure 3b). From the TG/DTG curves shown in Figure 3c, the contents of S in the nanocomposites were determined to be ca. 50 and 77 wt%, which were denoted as GSH@APC-S-55, 77 respectively. A strong interaction between sulfur and GSH@APC was confirmed by the improved thermal stability of S nanofillers compared with pure sublimed powders. As detected from the X-ray diffraction (XRD) patterns and Raman spectra, GSH@APC-S-50 nanocomposites exhibited nearly identical spectral characteristics with GSH@APCs and no distinct intrinsic peak of sulfur was observed (Figure 3d and 3e). The as-impregnated sulfurs were well dispersed in almost amorphous state. The pristine GSH exhibited two distinct reflection peaks around 26.2° and 44.7°, which corresponded to the periodically arranged (002) and (100) plane of graphitic domain, respectively. However, the characteristic peaks of graphitic domain in carbon/sulfur composites showed slightly decreased intensity and broadened profile, which was another evidence of the intimate interplay between sulfur guest and carbon host. Furthermore, the GSH@APC-S-50 nanocomposites possessed much lower specific surface area and nearly all the micro-/small-mesopores were occupied by S after the S impregnation (Figure 3f and Table 1), indicating the conspicuous utilization of S-storage reservoir. Considering the size compatibility between cyclo-S_8 molecules (0.76 nm)[23] and pores (>7 nm), it was inferred that the sulfur were mainly in the form of nanoscale cyclo-S_8 molecular clusters which were uniformly distributed and encapsulated in the hierarchical GSH-core/porous APC-shell matrix with the strong special confinement of 0.5–5 nm pores. However, as indicated by XRD pattern (Figure 3d) and the high-resolution TEM (HR-TEM) image of GSH@APC-S-77 (Figure S8), whether the slightly weak but sharp diffraction peaks of S or exposed (222) plane with d-spacing of 0.385 nm demonstrated that a portion of bulk S_8 particles transferred into S_8 nanocrystals, which were mainly accommodated in larger mesopores.

The electrochemical performance of the GSH@APC-S cathode for Li-S cells was investigated by cyclic voltammogram (CV), galvanostatic charge-discharge measurement, and electrochemical impedance spectroscopy (EIS) measurement. As shown in the first cathodic scan of the CV profiles (**Figure 4**a), two main reduction peak around 2.34 and 2.07 V was clearly presented, corresponding to the transformation from cyclo-S_8 to high-order lithium polysulfides (Li_2S_x, x = 4–8) and the sequential reduction of high-order lithium polysulfides into lithium sulfide (Li_2S_2 and Li_2S). In the subsequent anodic scan, only one strong oxidation peak around 2.37 V was observed, which associated to the coupled conversion from lithium sulfide to lithium polysulfides, and ultimately to element sulfur. Both the reduction and oxidation peaks were slightly shifted

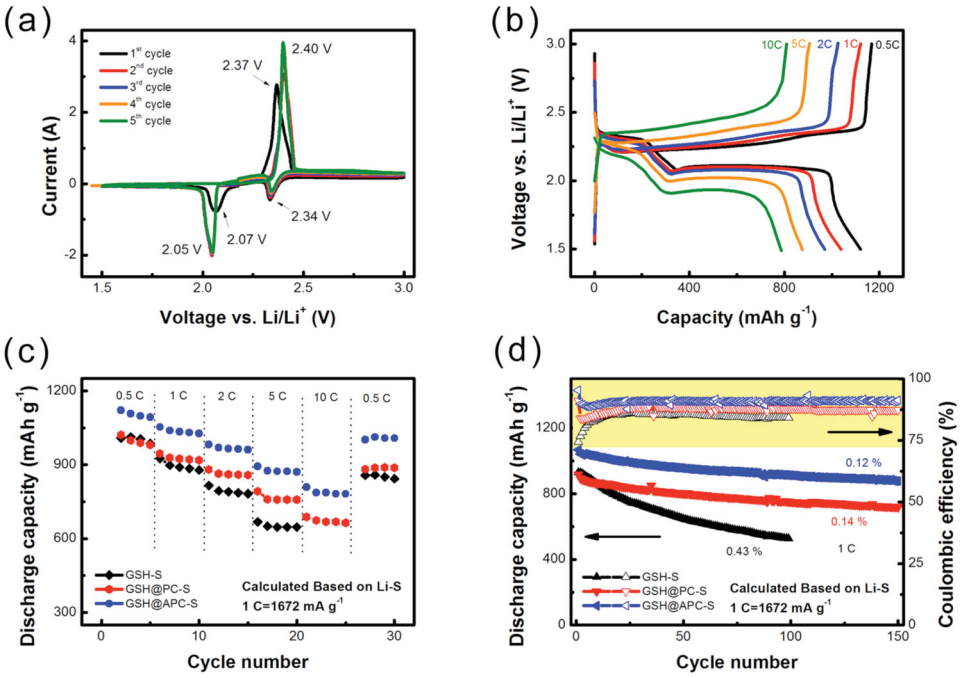

Figure 4. The electrochemical performance of GSH@APC-S-50 cathode: (a) CV profiles; (b) Galvanostatic charge-discharge curves at different current density; (c) Rate performance and (d) cycling performance at current density of 1 C (compared with GSH-S, GSH@PC-S cathode materials in which the contents of S were ca. 50 wt%).

in the next four cycles, suffering stronger polarization of the electrode materials. This can be ascribed to the increased viscosity of the electrolyte induced by the dissolution of lithium polysulfides during the 1st discharge. However, no remarkable changes can be detected for both the anodic/cathodic peaks in the 2nd to 5th cycles, indicating the high electrochemical stability of the GSH@APC-S cathode coupling with the universal electrolyte composed of lithium bis(trifluoromethanesulfonyl) imide (LiTFSI)-solute and 1,3-dioxolane (DOL)/1,2-dimethoxyethane (DME)-double-solvents.

The high capacity reversibility of the GSH@APC-S cathode was also confirmed in the charge-discharge curves (Figure 4b). When the current rate was 0.5 C, there were two voltage plateaus at ~2.23 and ~2.10 V in the discharge process, which can be roughly assigned to the two-step quasi-dynamic-equilibrium reaction of sulfur and lithium. Besides, a reversible capacity of 1121 mAh g^{-1} was achieved and gradually decreased at the evaluated current density (Figure 4c). Though severer polarization and distortion emerged with increasing the current density as indicated by the charge-discharge curves (Figure 4b), a high reversible capacity of 810 mAh g^{-1} was still preserved even at a high rate of 10 C, which was much higher than GSH-S (668 mAh g^{-1} at 5 C) and GSH@PC-S (689 mAh g^{-1} at 10 C) with same electrolyte and similar content of S. The recovery of a reversible capacity of 1002 mAh g^{-1} can also be achieved at 0.5 C following the high-C charge-discharge process (Figure 4c). Thus, GSH@APC-S nanocomposite cathode with such favorable high-rate performance and electrochemical reversibility can be among the-state-of-art energy storage devices based on multiple-electron-transfer electrochemistry. Furthermore, the GSH@APC-S nanocomposites exhibited promising cycling performance contributed from the strongly-coupled carbon hosts and sulfur guests (Figure 4d and S10a,b). A cyclic capacity fading of 0.32% was detected during the first 20 cycles at current density of 1 C. This capacity decay was reduced to 0.088% of initial capacity per cycle with a relatively high capacity of 877 mAh g^{-1} after 150 cycles, while GSH-S and GSH@PC-S cathode materials obtained lower initial reversible capacity of 928 mAh g^{-1} (GSH-S)/916 mAh g^{-1} (GSH@PC-S) and relatively worse capacity retention of 0.14% (GSH-S)/0.43% (GSH@PC-S) decay per cycle during the 150 cycles. Such favorable cycling performance can be attributed to the high stability of GSH@APC nanostructure illustrated by TEM images of cathode surface morphology (Figure S9), in which the essential conductive matrix was well preserved. In addition, note that in the as-fabricated Li-S cell, $LiNO_3$-additive-free LiTFSI-DOL/DME electrolyte system can only provide extremely weak protection to Li anode through the formation of instable solid-electrolyte-interface film, the coulombic efficiency of GSH@APC-S cathode (ca. 91%) showed no obvious change and was also higher than GSH-S (ca. 84%) and GSH@PC-S (ca. 87%), indicating that the typical shuttling phenomenon was strictly prevented via the formation of small cyclo-S_8 molecular clusters strongly confined in abundant micro-/mesopores. Such improved electrochemical performance in both fast charge-discharge capability and cycling performance was further demonstrated via Nyquist plot and its fitted results of equivalent circuits (Figure S10c and Table S1). Cells with GSH@APC-S-50 cathode embodied much decreased impedance of electrolyte and cell components (R_s = 1.96 Ω) than GSH-S cathode (R_s = 7.25 Ω), which can be ascribed the

DOI: 10.1002/adfm.201303296

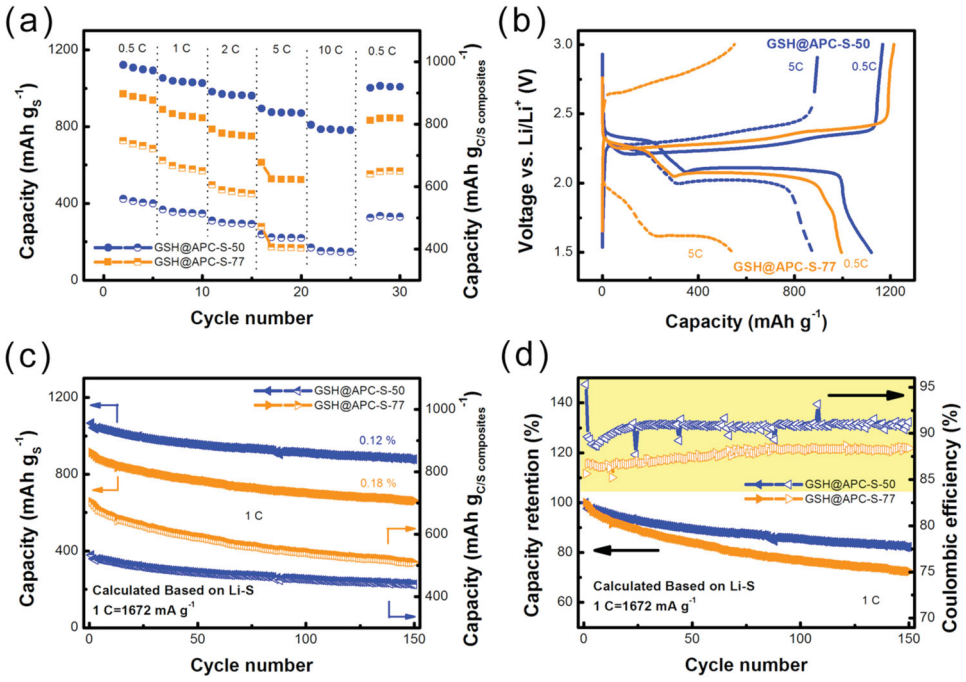

Figure 5. The electrochemical performance of GSH@APC-S-50,77 cathode: (a) Rate performance, (b) galvanostatic charge-discharge curves at different rate, (c) cycling performance at current density of 1 C (calculation of discharge capacity was based on both mass of S and the whole cathode material), and (d) coulombic efficiency and capacity retention at current density of 1 C.

stronger entrapment and less dissolution of polysulfides, as well as further decreased viscosity of the electrolyte after porous carbon introduced. Meanwhile, enhanced rate performance was available due to the lower electron/ion transfer resistance as charge-transfer impedance (R_{ct}) and infinite length Warburg element (W_o) illuminated, which was originated from the high electronic conductivity of 29.3 S cm^{-1} and well-tailored nanostructure. Furthermore, note that the GSH@PC-S possessing lower specific surface area and bulk conductivity than the GSH-S exhibited better Li-storage performance. The possible reason was ascribed to the enhanced affinity of sulfur with carbon surface due to the abundant defects, edges and oxygen functional groups introduced by turbostratic carbon layer in the GSH@PC. This was in good accordance with the high thermal stability of sulfur in the GSH@PC-S than the GSH-S (Figure S11). The effects of surface defects and functional groups need to be further investigated.

As the S loading increased from 50 to 77 wt%, discharge capacities of 970/613 mAh g^{-1} at rate of 0.5/5 C can still be achieved (**Figure 5**a) even though charge-discharge curves of GSH@APC-S-77 cathode endured more serious polarization with the increase of intrinsically insulative S and its evolutionary products (Figure 5b). Considering such extremely high S loading and no assistance of any other conductive agent, such as carbon black and CNTs, to provide extra electron pathway, the outstanding rate performance of GSH@APC-S-77 nanocomposites was mainly attributed to the 3D connected scaffolds with extraordinary conductivity constructed with GSH frameworks. Meanwhile, a high initial capacity of 914 mAh g^{-1} was available at current density of 1 C; while after 150 cycles, over 72% of initial capacity was well preserved (Figure 5c). However, compared with the relatively low S loading samples, GSH@APC-S-77 cathode suffered from half faster cyclic capacity fading of 0.18%. This is obviously lower than the value reported on the mesoporous carbon (0.65%),[28] CNT (0.41%),[14] graphene (0.26%),[26] hybrid (0.43%)[16] with high S loading based compostied cathodes. However, a portion of bulk S_8 particles was transformed into S_8 nanocrystals rather than small molecular clusters with such massive boost of S loading in the nanocomposites, which was in good accordance with XRD patterns and TEM images. Such S_8 nanocrystals were more accessible to electrolyte and corresponding soluble polysulfides cannot be effectively entrapped by porous carbon, thus leading to lower coulombic efficiency and worse capacity retention (Figure 5d). In spite of slightly lower capacity based on active mass and more instable cyclability, no surprisingly, such nanostructured GSH@APC-S composite with higher S loading exhibited better performance when evaluated via capacities based on total mass of C/S composites. In a desirably wide range of current density (<5 C), capacities based on composites of GSH@APC-S-77 were almost 20–40% higher than GSH@APC-S-50 (Figure 5a,c). In fact, the actual content of S in the binder-included cathode reached as high as 69.3 wt%, which can be one of the highest reported value as with spherical ordered mesoporous carbon (58.8 wt%),[28] SWCNT (50.4 wt%),[14] fibrous graphene (60 wt%),[26] reduced graphene oxide (63.9 wt%),[25] large-volume mesoporous carbon (67.2 wt%),[29] and S@reduced graphene oxide (68.3 wt%).[35] Compared to aforementioned high S loading cathodes, the GSH@APC-S cathodes still exhibited outstanding multiple-electron-transfer capability at huge current

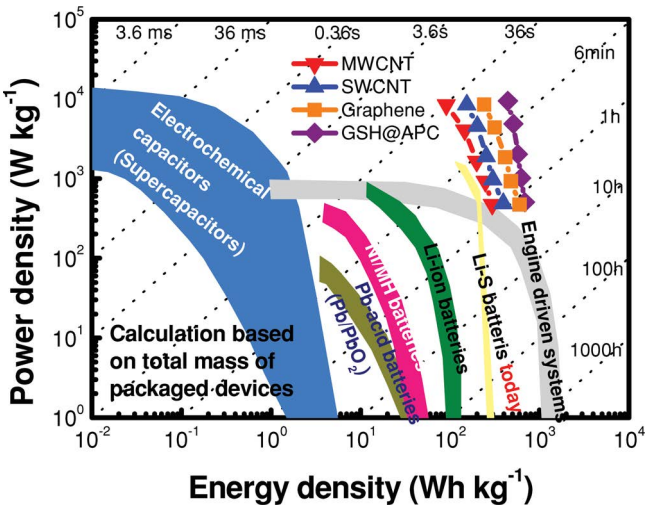

Figure 6. Ragone plot of the Li–S battery based on diverse sp^2 nanocarbon cathode materials (GSH@APC, graphene,[15] SWCNT and MWCNT),[14] as well as other energy storage devices (all based on total mass of packaged device).

densities over 1 C. On one hand, gravimetric and volumetric energy density were available with high S loading due to the increase of active mass and packaged density; on the other hand, good rate performance ensured its potential applications for high-power devices.

Our strategy towards the GSH@APC nanocomposites with hierarchical nanostructure was proved to be efficient and effective for Li-S battery with high efficiency and stability, exhibiting versatile advantages in both high energy density and power density via Ragone plots (**Figure 6**). When assembled into a packaged Li–S cell, such hierarchical composites offered much improved Li ion storage performance than SWCNT-S,[14] MWCNT-S,[14] or Graphene-S[15] cathodes reported in literatures, as the active electrode materials were about 35–40% of the total packaged mass considering lithium anodes, membranes and electrolytes.[36] Meanwhile, compared with Ni-MH batteries and commercial Li-ion battery, a much higher gravimetric energy density was achieved, while the gravimetric power density can also retain at the level of supercapacitors. For instance, gravimetric energy density based on the packaged GSH@APC-S//Li cell was expected to be 400 Wh kg^{-1} at a packaged power density of 10 000 W kg^{-1}, which was close to engine driven systems. Such good combination of CVD-grown GSHs and chemical-tailored APC into novel hierarchical core/shell nanostructure rendered its promising application as versatile cathode with high energy density and power density and its potential extension to prospective electrical transportation can be also expected.

Our results indicate the strategy for the fabrication of promising hierarchical nanoarchitectures for the Li–S batteries. The rational hybridization of the sp^2 nanocarbon with nanostructured carbon renders the composites with following outstanding advantages: (1) the CNT/graphene interlinked network offers high electrical conductivity for the composite cathode; (2) the APC shell introduces micro-/mesoporosity, together with the interlamellar compartments between the opposite graphene flakes, as the abundant electrochemical nanoreactors to accommodate sulfur and polysulfides; (3) the interconnected porous structures provide accessibility for liquid electrolyte to active materials; (4) the strong special confinement effect of the micro-/mesopores of GSH@APC renders the transformation of S_8 crystal into amorphous cyclo-S_8 molecular cluster, restraining the shuttle-phenomenon for a high capacity retention of Li–S cell; (5) the GSH/APC provides a stable framework to sustain the strain generated by the volumetric changes of the active materials during cycling, which assures the intact wire-up framework during the repeated charge and discharge. To obtain the all-carbon composites with unprecedented Li ion storage performance, it is highly recommended the amount of APC should be carefully tailored by the CVI time and chemical activation procedures. If the catalyst flakes were removed before CVI, or too much PC was deposited on the GSH framework, or too harsh conditions were employed, the electrical conductive scaffolds were lost and the structural stability was no longer preserved. Such hierarchical nanostructure loss deduced the capacity and stability of Li ion storage performance, as shown in Figure S12,13. Benefiting from the sufficient utilization of the intrinsic properties of well-dispersed graphene and SWCNTs with fractional defects due to the high-temperature generation, a Li–S cell with superior rate performance and high power density was available.

3. Conclusions

A hierarchical all-carbon nanostructure in which the porous carbon were in situ fabricated on an electrical conductive graphene/CNT hybrid scaffold was fabricated. The sp^2 graphene/CNT interlinked networks rendered the composites with good electrical conductivity and robust framework to sustain the strain generated by the volume changes of the active materials, while the micro-/mesoporous carbon and the interlamellar compartment between the opposite graphene served as electrochemical nanoreactor to accommodate sulfur and polysulfides. Their interconnected porous structures also provided the accessibility for liquid electrolyte to active materials. The strong special confinement of GSH@APC rendered the transformation of S_8 crystal into amorphous cyclo-S_8 molecular cluster, restraining the shuttle-phenomenon. The strong coupling between the sp^2 nanocarbon and porous carbon rendered the composite cathode with an ultrahigh specific capacity of 1121 mAh g^{-1} at 0.5 C, a favorable high-rate capability of 809 mAh g^{-1} at 10 C, a very low capacity decay of 0.12% per cycle, and an impressive cycling stability of 877 mAh g^{-1} after 150 cycles at current density of 1 C. As S loading increasing from 50 wt% to 77 wt%, high capacities of 970, 914, and 613 mAh g^{-1} were available at current densities of 0.5, 1, and 5 C respectively. Based on the total mass of packaged devices, gravimetric energy density of GSH@APC-S//Li cell was expected to be 400 Wh kg^{-1} at a power density of 10 000 W kg^{-1}, matching the level of engine driven systems. In addition, this work also offers a general strategy to combine the sp^2 nanocarbon with nanostructured carbon, which is crucial for illustrating the potential of carbon for advanced energy storage, probing the role of conductive robust network as

DOI: 10.1002/adfm.201303296

well as interconnected pores, and understanding the dynamic changes on the electrode. This approach may also be applicable for supercapacitor, Li ion batteries, Li air batteries, fuel cell systems that require electrodes with high electrical conductivity and tunable porous structures.

4. Experimental Section

Catalyst Preparation: The FeMoMgAl LDH flakes were prepared using a urea-assisted co-precipitation reaction. $Fe(NO_3)_3{\bullet}9H_2O$, $Mg(NO_3)_2{\bullet}6H_2O$, $Al(NO_3)_3{\bullet}9H_2O$, $Na_2MoO_4{\bullet}2H_2O$, and urea were dissolved in deionized water (1000 mL) with $[Mg^{2+}] + [Al^{3+}] = 0.15$ mol L^{-1}, n(Fe) : n(Mg) : n(Al) : n(Mo) = 0.1 : 2 : 1 : 0.01, and [urea] = 3.0 mol L^{-1}. The solution was kept at 94 °C under continuous magnetic stirring for 12 h in a 2000 mL flask (equipped with a reflux condenser) under ambient atmosphere. The as-obtained suspension was then filtered and the residue was washed by deionized water. After freeze-drying, the final products were ground to be brown-yellow powders, which were used as the catalyst for the growth of GSHs.

Synthesis of GSH@APC: The synthesis of GSH/GSH@PC was carried out using a one/two-step high-temperature catalytic CVD. Typically, the FeMoMgAl LDH flakes were sprayed uniformly into a quartz boat, which was then placed at the center of a horizontal quartz tube inserted into a furnace at atmospheric pressure. The furnace was then heated under Ar atmosphere with a flow rate of 400 mL min^{-1}. On reaching 950 °C, CH_4 (400 mL min^{-1}) was introduced into the reactor for 20 min (Step I). The as-obtained products were labeled as GSH/LDO. After that, the furnace was cooled down to 760 °C under Ar flow. Then, C_2H_4 (200 mL min^{-1}) was introduced into the reactor for 10 min to form pyrolytic carbon layer on the GSH (Step II). The as-obtained products were labeled as GSH@PC/LDO. After that, the furnace was cooled down to room temperature under Ar flow. Then, chemical activation was performed by physically mixing KOH with GSH@PC powders with a KOH/GSH@PC/LDO mass ratio of 2:1 and a heat treatment temperature of 750 °C in a Ar flow (100 mL min^{-1}). After activation, the as-obtained products were purified by HCl (1 mol L^{-1}) aqueous solution at 80 °C for 3 h and NaOH (6 mol L^{-1}) aqueous solution at 150 °C for 6 h, subsequently, to remove the FeMoMgAl LDO flakes. The GSH/LDO, GSH@PC/LDO were also treated with HCl and subsequent NaOH solution to remove LDO flakes. Finally, the as-obtained GSH, GSH@PC, and GSH@APC samples were filtered, washed, and freeze-dried for further characterizations.

Fabrication of GSH@APC-S Nanocomposites: The GSH@APC-S nanocomposites were fabricated with a typical melt-diffusion strategy. The GSH@APCs were firstly mixed with S powder with a mass ratio of 1 : 1.5 and 5 by milling for fabrication of GSH@APC-S-50, 77 respectively. The mixture was then placed in a sealed flask at 155 °C for 4 h to incorporate the S into the GSH@APCs.

Characterizations: The morphology of the samples were characterized by a JSM 7401F (JEOL Ltd., Tokyo, Japan) SEM operated at 3.0 kV and a JEM 2010 (JEOL Ltd, Tokyo, Japan) TEM operated at 120.0 kV. X-ray diffraction (XRD) patterns were recorded on a Bruker D8 Advance diffractometer at 40.0 kV and 120 mA with Cu-Kα radiation. The pore-size distribution and BET specific surface area of the samples were measured by N_2 adsorption/desorption using Autosorb-IQ2-MP-C system. The pore size distribution and pore volume of the nanocarbon samples were calculated by the quenched solid state functional theory (QSDFT) method. Raman spectra were recorded with He-Ne laser excitation at 633 nm using Horiba Jobin Yvon LabRAM HR800 Raman Spectrometer. The TGA was carried out on the samples using TGA/DSC1 STAR^e system under O_2 and N_2 atmosphere, respectively. The resistance measurements of the GSH@APC disk were performed using the KDY-1 four-probe technique.

GSH@APC-S Cathode for Li–S Batteries: Two-electrode cells using standard 2025 coil-type cells were constructed to evaluate the electrochemical performance of the GSH@APC as the cathode material for Li-S batteries. The GSH@APC-S cathode slurry was prepared by mixing 90% of the GSH@APC-S nanocomposites and 10% of the poly(vinylidene fluoride) binder in a N-methyl-pyrrolidone (NMP) solvent dispersant. The positive electrodes were fabricated by coating the slurry on aluminum foil and drying at 60 °C for 24 h. Two different electrolytes were used in the electrochemical evaluation. A 1 mol L^{-1} LiTFSI solution in DOL:DME (v/v = 1:1) was used for electrochemical evaluation. Lithium metal foil was used as the anode and the polypropylene membranes from Celgard Inc. were used as the separators. The coin cells were tested in galvanostatic mode at various currents within a voltage range of 1.5–3.0 Vusing Neware multichannel battery cycler. The CV and EIS measurements were performed on Solartron 1470E electrochemical workstation at a scan rate of 0.1 mV s^{-1}. A current density of 1672 mA g^{-1} (1 C) equivalent to full discharge or charge in one hour was applied in both current sweep directions. The capacities were calculated based on the mass of sulfur.

Supporting Information

Supporting Information is available from the Wiley Online Library or from the author. It includes SEM data, TEM data, and electrochemical performances of composite cathode for Li–S batteries.

Acknowledgements

The work was supported by the Foundation for the National Basic Research Program of China (No. 2011CB932602), China Postdoctoral Science Foundation (2012M520293, 2013T60125), and National Natural Science Foundation of China (21306103). We thanks Xiao-Fei Liu and Wan-Cheng Zhu for helpful discussion.

Received: September 24, 2013
Revised: November 25, 2013
Published online:

[1] D. S. Su, R. Schlogl, *ChemSusChem* **2010**, *3*, 136–168.
[2] a) B. Luo, S. M. Liu, L. J. Zhi, *Small* **2012**, *8*, 630–646; b) Y. Huang, J. J. Liang, Y. S. Chen, *Small* **2012**, *8*, 1805–1834; c) H. Wang, H. Dai, *Chem. Soc. Rev.* **2013**, *42*, 3088–3113; d) S. Han, D. Q. Wu, S. Li, F. Zhang, X. L. Feng, *Small* **2013**, *9*, 1173–1187.
[3] Y. P. Zhai, Y. Q. Dou, D. Y. Zhao, P. F. Fulvio, R. T. Mayes, S. Dai, *Adv. Mater.* **2011**, *23*, 4828–4850.
[4] a) C. Liu, F. Li, L. P. Ma, H. M. Cheng, *Adv. Mater.* **2010**, *22*, E28–62; b) Q. Zhang, J.-Q. Huang, W.-Z. Qian, Y.-Y. Zhang, F. Wei, *Small* **2013**, *9*, 1237–1265.
[5] X. M. Fan, C. Yu, Z. Ling, J. Yang, J. S. Qiu, *ACS Appl. Mater. Interfaces* **2013**, *5*, 2104–2110.
[6] L. Zhang, F. Zhang, X. Yang, G. K. Long, Y. P. Wu, T. F. Zhang, K. Leng, Y. Huang, Y. F. Ma, A. Yu, Y. S. Chen, *Sci. Rep.* **2013**, *3*, 1408.
[7] E. Raymundo-Pinero, M. Cadek, M. Wachtler, F. Beguin, *ChemSusChem* **2011**, *4*, 943–949.
[8] Z. S. Wu, Y. Sun, Y. Z. Tan, S. B. Yang, X. L. Feng, K. Mullen, *J. Am. Chem. Soc.* **2012**, *134*, 19532–19535.
[9] X. C. Zhao, Q. Zhang, C. M. Chen, B. S. Zhang, S. Reiche, A. Q. Wang, T. Zhang, R. Schlogl, D. S. Su, *Nano Energy* **2012**, *1*, 624–630.
[10] Y. Yan, Y. X. Yin, S. Xin, Y. G. Guo, L. J. Wan, *Chem. Commun.* **2012**, *48*, 10663–10665.
[11] S. Xin, L. Gu, N. H. Zhao, Y. X. Yin, L. J. Zhou, Y. G. Guo, L. J. Wan, *J. Am. Chem. Soc.* **2012**, *134*, 18510–18513.
[12] S. Lu, Y. Cheng, X. Wu, J. Liu, *Nano Lett.* **2013**, *13*, 2485–2489.

[13] a) W. D. Zhang, I. Y. Phang, T. X. Liu, *Adv. Mater.* **2006**, *18*, 73–77; b) Q. Zhang, M. Q. Zhao, Y. Liu, A. Y. Cao, W. Z. Qian, Y. F. Lu, F. Wei, *Adv. Mater.* **2009**, *21*, 2876–2880; c) M. Q. Zhao, Q. Zhang, X. L. Jia, J. Q. Huang, Y. H. Zhang, F. Wei, *Adv. Funct. Mater.* **2010**, *20*, 677–685; d) M. Q. Zhao, Q. Zhang, J. Q. Huang, F. Wei, *Adv. Funct. Mater.* **2012**, *22*, 675–694.
[14] S. M. Zhang, Q. Zhang, J. Q. Huang, X. F. Liu, W. C. Zhu, M. Q. Zhao, W. Z. Qian, F. Wei, *Part. Part. Syst. Char.* **2013**, *30*, 158–165.
[15] J. Q. Huang, X. F. Liu, Q. Zhang, C. M. Chen, M. Q. Zhao, S. M. Zhang, W. C. Zhu, W. Z. Qian, F. Wei, *Nano Energy* **2013**, *2*, 314–321.
[16] M. Q. Zhao, X. F. Liu, Q. Zhang, G. L. Tian, J. Q. Huang, W. C. Zhu, F. Wei, *ACS Nano* **2012**, *6*, 10759–10769.
[17] J. C. Wang, S. Kaskel, *J. Mater. Chem.* **2012**, *22*, 23710–23725.
[18] a) W. Xia, V. Hagen, S. Kundu, Y. M. Wang, C. Somsen, G. Eggeler, G. G. Sun, G. Grundmeier, M. Stratmann, M. Muhler, *Adv. Mater.* **2007**, *19*, 3648; b) Z. Y. Sun, N. N. Dong, K. P. Xie, W. Xia, D. Konig, T. C. Nagaiah, M. D. Sanchez, P. Ebbinghaus, A. Erbe, X. Y. Zhang, A. Ludwig, W. Schuhmann, J. Wang, M. Muhler, *J. Phys. Chem. C* **2013**, *117*, 11811–11817.
[19] Y. W. Zhu, S. Murali, M. D. Stoller, K. J. Ganesh, W. W. Cai, P. J. Ferreira, A. Pirkle, R. M. Wallace, K. A. Cychosz, M. Thommes, D. Su, E. A. Stach, R. S. Ruoff, *Science* **2011**, *332*, 1537–1541.
[20] a) P. G. Bruce, S. A. Freunberger, L. J. Hardwick, J. M. Tarascon, *Nat. Mater.* **2012**, *11*, 19–29; b) Y. Yang, G. Zheng, Y. Cui, *Chem. Soc. Rev.* **2013**, *42*, 3018–3032; c) A. Manthiram, Y. Z. Fu, Y. S. Su, *Accounts. Chem. Res.* **2013**, *46*, 1125–1134.
[21] a) S. Evers, L. F. Nazar, *Accounts. Chem. Res.* **2013**, *46*, 1135–1143; b) D. W. Wang, Q. C. Zeng, G. M. Zhou, L. C. Yin, F. Li, H. M. Cheng, I. Gentle, G. Q. Lu, *J. Mater. Chem. A* **2013**, *1*, 9382–9394; c) L. M. Suo, Y. S. Hu, H. Li, M. Armand, L. Q. Chen, *Nat. Comm.* **2013**, *4*, 1481.
[22] a) G. M. Zhou, D. W. Wang, F. Li, P. X. Hou, L. C. Yin, C. Liu, I. Gentle, G. Q. Lu, H. M. Cheng, *Energy Environ. Sci.* **2012**, *5*, 8901–8906; b) J. J. Chen, Q. Zhang, Y. N. Shi, L. L. Qin, Y. Cao, M. S. Zheng, Q. F. Dong, *Phys. Chem. Chem. Phys.* **2012**, *14*, 5376–5382.
[23] J. Guo, Y. Xu, C. Wang, *Nano Lett.* **2011**, *11*, 4288–4294.
[24] a) S. Evers, L. F. Nazar, *Chem. Commun.* **2012**, *48*, 1233–1235; b) L. W. Ji, M. M. Rao, H. M. Zheng, L. Zhang, Y. C. Li, W. H. Duan, J. H. Guo, E. J. Cairns, Y. G. Zhang, *J. Am. Chem. Soc.* **2011**, *133*, 18522–18525; c) H. Wang, Y. Yang, Y. Liang, J. T. Robinson, Y. Li, A. Jackson, Y. Cui, H. Dai, *Nano Lett.* **2011**, *11*, 2644–2647; d) C. Zu, A. Manthiram, *Adv. Energy Mater.* **2013**, *3*, 1008–1012.
[25] H. Sun, G. L. Xu, Y. F. Xu, S. G. Sun, X. F. Zhang, Y. C. Qiu, S. H. Yang, *Nano Res.* **2012**, *5*, 726–738.
[26] G. Zhou, L.-C. Yin, D.-W. Wang, L. Li, S. Pei, I. R. Gentle, F. Li, H.-M. Cheng, *ACS Nano* **2013**, *7*, 5367–5375.
[27] a) X. Ji, K. T. Lee, L. F. Nazar, *Nat. Mater.* **2009**, *8*, 500–506; b) F. G. Sun, J. T. Wang, H. C. Chen, W. C. Li, W. M. Qiao, D. H. Long, L. C. Ling, *ACS Appl. Mater. Interfaces* **2013**, *5*, 5630–5638.
[28] J. Schuster, G. He, B. Mandlmeier, T. Yim, K. T. Lee, T. Bein, L. F. Nazar, *Angew. Chem. Int. Ed.* **2012**, *51*, 3591–3595.
[29] D. Li, F. Han, S. Wang, F. Cheng, Q. Sun, W. C. Li, *ACS Appl. Mater. Interfaces* **2013**, *5*, 2208–2213.
[30] a) N. Brun, K. Sakaushi, L. H. Yu, L. Giebeler, J. Eckert, M. M. Titirici, *Phys. Chem. Chem. Phys.* **2013**, *15*, 6080–6087; b) C. F. Zhang, H. B. Wu, C. Z. Yuan, Z. P. Guo, X. W. Lou, *Angew. Chem. Int. Ed.* **2012**, *51*, 9592–9595; c) K. Zhang, Q. Zhao, Z. L. Tao, J. Chen, *Nano Res.* **2013**, *6*, 38–46.
[31] a) S. C. Wei, H. Zhang, Y. Q. Huang, W. K. Wang, Y. Z. Xia, Z. B. Yu, *Energy Environ. Sci.* **2011**, *4*, 736–740; b) B. Ding, C. Z. Yuan, L. F. Shen, G. Y. Xu, P. Nie, X. G. Zhang, *Chem. Eur. J.* **2013**, *19*, 1013–1019; c) C. D. Liang, N. J. Dudney, J. Y. Howe, *Chem. Mater.* **2009**, *21*, 4724–4730; d) S. Xin, Y. X. Yin, L. J. Wan, Y. G. Guo, *Part. Part. Syst. Char.* **2013**, *30*, 321–325.
[32] J. Shao, X. Y. Li, L. Zhang, Q. T. Qu, H. H. Zheng, *Nanoscale* **2013**, *5*, 1460–1464.
[33] a) J. L. Wang, J. Yang, C. R. Wan, K. Du, J. Y. Xie, N. X. Xu, *Adv. Funct. Mater.* **2003**, *13*, 487–492; b) L. C. Yin, J. L. Wang, F. J. Lin, J. Yang, Y. Nuli, *Energy Environ. Sci.* **2012**, *5*, 6966–6972.
[34] Y. Yang, G. H. Yu, J. J. Cha, H. Wu, M. Vosgueritchian, Y. Yao, Z. A. Bao, Y. Cui, *ACS Nano* **2011**, *5*, 9187–9193.
[35] H. Zhao, Z. Peng, W. Wang, X. Chen, J. Fang, J. Xu, *J. Power Sources*2014, *245*, 529–536.
[36] H. S. Choi, J. H. Im, T. Kim, J. H. Park, C. R. Park, *J. Mater. Chem.* **2012**, *22*, 16986–16993.